The Astrophysical Journal, 956:59 (13pp), 2023 October 10 https://doi.org/10.3847/1538-4357/acf28d

A Statistical Analysis of Deflection of Coronal Mass Ejections in the Field of View of LASCO Coronagraphs

Grzegorz Michalek[1], Nat Gopalswamy[2], Seiji Yashiro[2,3], and Kostadinka Koleva[2,3,4]
[1] Astronomical Observatory of Jagiellonian University, Krakow, Poland; grzegorz.michalek@uj.edu.pl
[2] NASA Goddard Space Flight Center, Greenbelt, MD, USA
[3] The Catholic University of America, Washington, DC 20064, USA
[4] Space Research and Technology Institute, Bulgarian Academy of Sciences, Poland
Received 2023 June 24; revised 2023 August 9; accepted 2023 August 19; published 2023 October 6

Abstract

Coronal mass ejections (CMEs) can generate the most severe geomagnetic disturbances. One of the most critical factors affecting a CME's geoeffectiveness is its trajectory. It is crucial to determine whether and when CME will hit Earth. It is commonly assumed that CMEs experience a deflection of propagation in the corona and in interplanetary space. In this study, we analyze more than 14,000 CMEs listed in the Coordinate Data Analysis Workshop (CDAW) catalog during 1996–2022 to estimate their deflection in the Large and Spectrometric Coronagraph field of view (LFOV). In our statistical analysis, the deflection was determined using the CME height–time measurements listed in the CDAW catalog. We have shown that, in the solar corona, CME deflection is a common phenomenon, heavily influenced by solar activity cycles as well as phases of these cycles. We have demonstrated that during periods of solar activity minima the deflection of CMEs is mostly toward the equator, and during periods of maxima it is mostly toward the poles. This general trend of deflection is further modified by the specific structure of the magnetic field generated during successive cycles of solar activity (e.g., the asymmetry between the hemispheres). A systematic increase in deflection with time was also recognized. We have also found that the deflection increases linearly with the distance from the Sun in the LFOV (the line slope is 0.5).

Unified Astronomy Thesaurus concepts: Active solar corona (1988); Solar coronal mass ejections (310)

1. Introduction

Coronal mass ejections (CMEs) are sudden and very energetic expulsions of magnetized plasma from the solar corona that can generate severe geomagnetic disturbances. The first white-light CME was detected in 1971 by the seventh Orbiting Solar Observatory (OSO-7; Tousey 1973) although CME substructures were known for a long time (see Gopalswamy 2016, for a review). Predicting space weather requires, among other components, a precise determination of the CME trajectory in the interplanetary medium. It was discovered by the initial space coronagraphs (Skylab and Solar Maximum Mission) that CME trajectories are deflected toward the solar equator (Hildner 1977; MacQueen et al. 1986). We now know that deflection depends on many factors and occurs in the vicinity of the Sun as well as in the entire interplanetary medium. Near the Sun, the deflection of CMEs can happen due to interactions with magnetic structures such as coronal holes (CH), streamers, current sheets, and other CMEs. The interaction between CMEs, resulting in the trajectory change of the preceding CME, was reported by Gopalswamy et al. (2001). During these collisions, CMEs can undergo significant deflection over a short period of time (Xiong et al. 2006, 2009; Lugaz et al. 2012, 2017; Mishra et al. 2017). It seems, however, that the most influential factor disturbing CME trajectories close to the Sun is the effect of CHs. Their structure is stable over long periods of time, so they can systematically influence ejection movement. In addition, CH location changes with solar activity cycles. The presence of a coronal hole may cause CME deflections toward (Gopalswamy et al. 2005) or away from (Gopalswamy et al. 2004) the ecliptic plane. Gopalswamy et al. (2003), on the basis of the spatial correspondence between solar prominence eruptions (PEs) and the CMEs, demonstrated that, during the solar minimum, the central position angle of the CMEs deviated toward the solar equator (Gopalswamy & Thompson 2000; Gopalswamy et al. 2003). Testing the structured CMEs, Cremades & Bothmer (2004) obtained the same result. Equatorward deflections can explain why CMEs originating at higher latitudes (up to 50°) are observed as magnetic clouds at 1 au during the rising phase of solar cycle 23 (Gopalswamy et al. 2008). On the other hand, considering driverless shocks, Gopalswamy et al. (2009) suggested that, during the declining solar phase of activity, the deflection can be in the longitudinal direction away from the line joining the coronal hole and eruption region. This is because, during the declining phase of solar activity, CHs occur at low latitudes deflecting CMEs away from the coronal holes. Using all CMEs listed in the Coordinated Data Analysis Workshop (CDAW) CME catalog during the low solar activity period (1997–1998), Wang et al. (2011) conducted an extended statistical analysis and confirmed that CMEs mostly deflect toward the solar equator. Mäkelä et al. (2013) studied the influence of physical parameters of CHs, such as area, average magnetic field strength, and distance from the CME location, to estimate the deflection value. The presented results show that deflections are clearly correlated with the relative locations of coronal holes and the heliospheric current sheet (HCS). The deflection motion is from the regions of the high density of magnetic energy (CHs) toward the places where the magnetic energy density reaches the minimum (HCS; Gui et al. 2011; Shen et al. 2011). It is commonly accepted that CMEs can undergo

significant latitudinal deflection (tens of degrees) below 5 $R_\odot$ (Wang et al. 2011), which may change the effectiveness of CMEs. In fact, the extent of deflection depends on many factors. Kay et al. (2015) found that slow, wide, low-mass CMEs in strong magnetic fields and magnetic gradients exhibit the largest deflections. Isavnin et al. (2014) demonstrated that latitudinal deflection due to magnetic energy density gradient occurs only below 30 $R_\odot$. However, the situation is not so simple.

The interplanetary medium still affects ejection trajectories. Wang et al. (2004) performed a statistical study of Earth-encountered front-side halo CMEs and found that the source distribution had east–west asymmetry that depended on CME speeds. They explained this effect as being due to the deflection in interplanetary space of CMEs propagating in the background spiral magnetic field. As a result, in such a background environment, faster interplanetary coronal mass ejections (ICMEs) are slowed down by the slow solar wind ahead and are deflected eastward, whereas slower ICMEs are accelerated by the faster solar wind behind and are deflected westward. Observing the propagation process of an isolated ICME, Wang & Colaninno (2014) showed that CMEs can be deflected significantly in the interplanetary space. Deflection for this particular event was greater than 20° toward the east. They concluded that deflection in the interplanetary space is due to interaction with the background solar wind. However, it is not due to the magnetic energy density gradient we observe in the corona. The interplanetary medium is filled with fast (from CHs) and slow (from streamers) solar winds. Corotating interaction regions (CIRs) resulting from the interaction of fast and solar winds are the most significant factors causing CME deflections in the interplanetary space (Prise et al. 2015). CMEs deflection in the interplanetary space is less violent than in the solar corona. However, it takes place in a much larger space and its cumulative effect is similar. Now, thanks to the Sun Earth Connection Coronal and Heliospheric Investigation (SECCHI; Howard et al. 2008) telescopes on board Solar TErrestrial RElations Observatory (STEREO; Kaiser et al. 2008), we can observe CMEs up to 1 au (Harrison et al. 2018). These observations revealed that deflections could be more complex and also occur in longitudes (Liu et al. 2010a, 2010b; Lugaz et al. 2010; Rodriguez et al. 2011; Isavnin et al. 2013; Kay & Gopalswamy 2017). The propagation of CMEs in the ambient solar wind is also commonly studied with magneto-hydrodynamic (MHD) simulations (e.g., Feng et al. 2003; Manchester et al. 2004; Shen et al. 2014; Kay et al. 2016; Zhou & Feng 2017). The MHD simulations performed by Zhou & Feng (2013) showed that the deflection of the CME depends not only on the background magnetic field but also on the initial magnetic field strength of CMEs. CMEs with an initial magnetic field parallel to the ambient field deflected toward the equator, but those with an antiparallel internal field deflected toward the poles. They also found an anticorrelation between the latitudinal deflection extent and the CME average transit speed and energy. Recently, Zhuang et al. (2019) have numerically considered CME deflection in the heliospheric equatorial plane. They demonstrated that the deflection of structured CMEs is correlated with the speed difference between the flux rope structure and the solar wind. Similar simulations, but taking into account the interaction with CIRs, have been performed by Liu et al. (2019). It was found that, without the CIR, the fast CME deflects eastward. However, when it hits the west flank of the CIR, it is still deflected eastward. Deflection angles are larger when CME interacts with the CIR than when CME interacts only with the solar wind.

We must also mention that the parameters, such as the electron density, temperature, and plasma β temperature play a key role in the dynamics of the solar atmosphere and propagation of CMEs near the Sun. Unfortunately, determination of these parameters is not easy, because the plasma in the solar corona is optically thin. Gómez et al. (2018) used the COronal DEnsity and Temperature (CODET) model to investigate some relevant aspects such as variations of density and temperature through the solar corona during solar cycles 23 and 24. They demonstrated that temperature (inversely proportional to the magnetic field) and electron density (proportional to the magnetic field) are strongly dependent on the magnetic field magnitude. Therefore, cycle 23 was characterized by lower temperature values than solar cycle 24. Higher values in the density profiles were more frequently recorded during solar cycle 23 as compared to solar cycle 24. Gómez et al. (2019) used the same model to study the plasma β variations through the solar corona during solar cycles 23 and 24. This parameter strongly depends on the magnetic field, density, and temperature in the solar corona, as well. An interesting behavior of plasma β was observed during the last solar cycles. Above active regions, higher values of β were observed in solar cycle 23 compared to solar cycle 24. But in faculae and quiet Sun (QS) regions, the opposite trend was observed. The solar cycle 24 is characterized by lower magnetic activity, but the presence of higher values in plasma β for faculae and QS suggests that, during solar cycle 24, these features are predominant and can determine solar corona dynamics.

In the current study, we analyze only deflections within the LFOV. For this purpose, we use manually obtained height–time measurements of all CMEs included in the CDAW catalog in the period from 1996 to 2022. In particular, we study the evolution of the deviation with distance from the Sun and with solar activity cycles. We also test the influence of the basic CME attributes on the deflection extent. To make such an analysis, we only considered CMEs that attain a height of at least 10 $R_\odot$.

The paper is organized as follows. In Section 2, we briefly present information about our data and method. Section 3 includes our study results. We summarize the results in Section 4.

2. Data and Method

Thanks to the sensitive Large and Spectrometric Coronagraph (LASCO) on board the Solar and Heliospheric Observatory (SOHO), we have been observing CMEs almost continuously up to a distance of 32 $R_\odot$ (Brueckner et al. 1995). These observations cover more than two cycles of solar activity (1996–2022). The observed kinematic attribute CMEs are stored in the SOHO/LASCO catalog (Yashiro et al. 2004; Gopalswamy et al. 2009b). By the end of 2022, this catalog contained over 30,000 CMEs. It is the only catalog where identification and height–time measurements are made by a human observer. The height–time measurements made for this catalog form the basis of our considerations. For the current research, the most significant thing is that successive height–time measurements were carried out for the fastest structure extracted from a given event. The position of this structure is determined by two parameters: the distance from the Sun

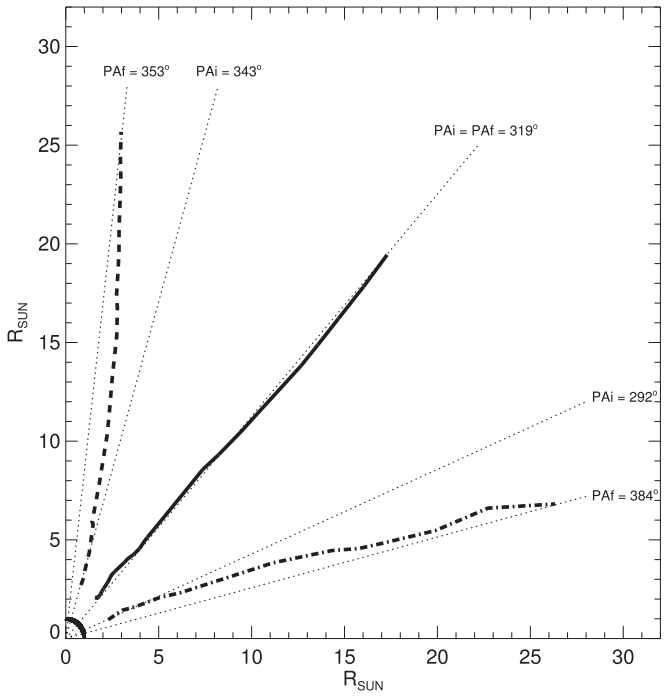

Figure 1. Sample trajectories of three CMEs (distance from the Sun vs. PA) illustrate deflection toward the equator (dotted line, 20010819.060605), the pole (dashed line, 20040519.202605), and no deflection (continuous line, 20100413.083005). The dotted lines indicate the initial and final PAs of the respective CMEs. Figure illustrates the field of view of LASCO coronographs for position angles from 270° to 360°. In the bottom left corner, the solar surface is marked.

expressed in $R_\odot$ and the position angle (PA). PA is measured counterclockwise from solar north in degrees (0°–360°). In the current study, we are only interested in latitudinal deflection; therefore, the CME position angles have been converted to absolute values of their latitude (|latitude| = [0°–90°]). Such a method to obtain CME latitudes from CME central position angle has been used in the past in studying solar polarity reversal (Gopalswamy et al. 2003a). The catalog also includes the central position angle (CPA, in the range 0°–360°, measured counterclockwise starting from the north pole) that allows us to accurately locate a given CME on the solar disk. CPA is defined as the intersection between two CME edges. These edges are determined when a CME reaches its largest angular size. They are also used to estimate the CME apparent width. We may assume that this fastest structure follows the CME trajectory well. Therefore, having successive distances from the Sun and position angles for this structure, we can track the deflections of a given ejection in the LFOV. To study changes in deflection with distance from the Sun, we only used CMEs observed at a distance of at least $10R_\odot$. About 50% of all ejections in the catalog (14,349) meet this condition. For each considered ejection, we determine the position angle (PA) at the moment of its first appearance in the LFOV (PAi), at a distance of $5\,R_\odot$ (PA05), $10\,R_\odot$ (PA10), if possible, at a distance of $20\,R_\odot$ (PA20), and for the final measurement (PAf). For our analysis, all these position angles are taken as absolute angular distances from the equator. Having determined the position angles in this way, we can easily estimate the deflection angle at different distances from the Sun. As the basic value of the deflection angle, we will take the difference between PAi and PAf (DEF = PAi-PAf). In our analysis, we used only LASCO coronagraph images. They reflect CME trajectories projected onto the sky plane. Therefore, we can only use these data to study latitudinal deflection. The deflection will be determined by the angular value of the deviation of the ejection trajectory from the radial direction in the sky plane and the direction of this deviation. We assume that the deviation is positive when the CME trajectory turns toward the solar equator and negative when it deviates toward the solar poles. To illustrate the methodology in Figure 1, we present examples of events with deflection toward the equator, pole, and no deflection. The deviation of the trajectory toward the equator (ecliptic plane) will increase the chances of the event being geoeffective. Negative deviation means that the event is moving away from the ecliptic plane and its impact on our planet may be not significant. Manual measurements can introduce random errors. Therefore, we did not focus on a particular CME, but we performed an extensive statistical analysis of deflections. Because we have a very large sample of CMEs, such a statistical approach is well justified. The results of these studies are presented in the following subsections.

3. Results

The SOHO/LASCO catalog contains three basic attributes of CMEs (speed, width, and CPA) that can affect the ejection trajectory. Below, we present an analysis of the impact of these parameters on deflections.

3.1. Deflection Distribution

The large population of considered CMEs allows us to analyze the deflection distribution. Deflection near the Sun depends on complex magnetic structures in the solar corona. We expect that the final deflection is the accumulation of many independent interactions with magnetic structures. These structures may have different distributions depending on the solar cycle. Therefore, we should expect that the distribution of deflection in at least one cycle of solar activity should be close to the normal distribution. Figure 2 shows the deflection distributions for all considered CMEs (panel (a)), all CMEs in solar cycle 23 (panel (b)), and all CMEs in solar cycle 24 (panel (c)). In the upper left corner of each panel, the basic parameters of these distributions are presented. As expected, the deflection distribution of CMEs is normally distributed with a peak around 0°, regardless of whether we consider all events or separately for both cycles of solar activity (it is assumed that deflection has a normal distribution when mode≈mean≈median and kurtosis is lower than 3). It can also be seen that the maximum values of deflection, determined in the field of view of LASCO coronagraphs, are in the range ±30°. Two significant results are worth noting. First, in cycle 24 there were 12% less ejections reaching $10\,R_\odot$, compared to cycle 23, although for all recorded ejections the trend is opposite. This means that we observed a lot of CMEs in cycle 24 but they disappeared from the LFOV sooner than those in cycle 23. Second, the full width at half maximum (FWHM) of the deflection distributions is significantly different in both cycles. In cycle 24, the FWHM (18.°6) of deflection distributions was almost twice as large as that in cycle 23 (11.°4). This means that in cycle 24 the CMEs were much more deviated from the radial trajectory than in cycle 23. This result also indicates that the physical parameters of the CMEs in the two cycles were different. In solar cycle 24, the interplanetary medium was significantly rarefied after a deep and prolonged minimum

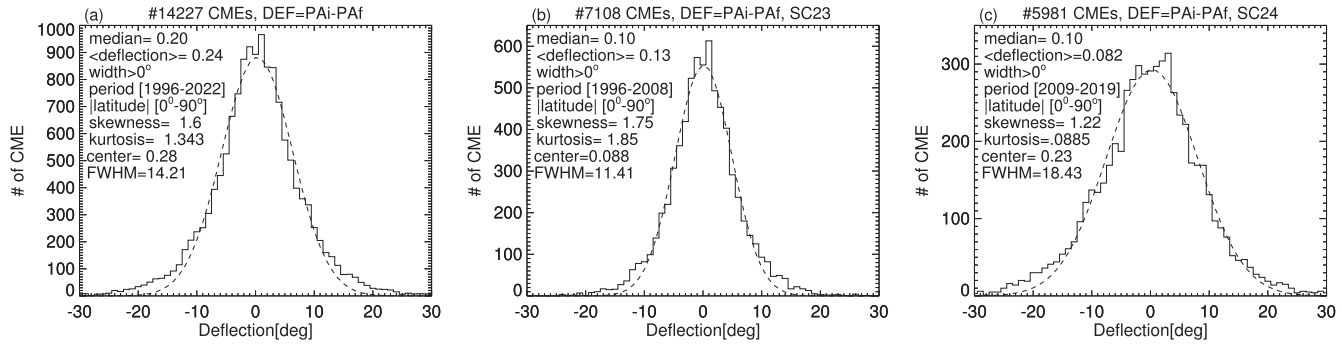

Figure 2. Deflection distributions (PAi-PAF) for all considered CMEs (panel (a)), all CMEs in solar cycle 23 (panel (b)), and all CMEs in solar cycle 24 (panel (c)). In the upper left corner of each panel, the basic parameters of these distributions are presented. Dashed lines represent a Gaussian fitting to histograms obtained from observations.

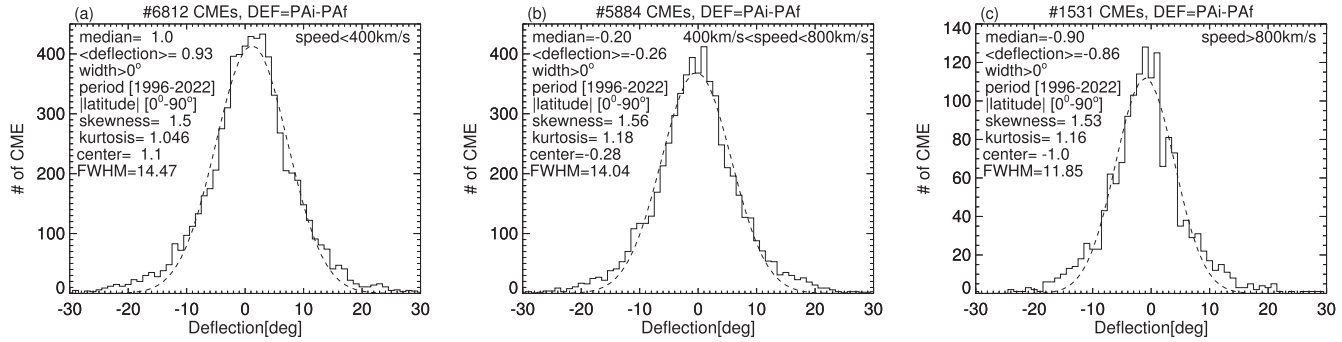

Figure 3. Deflection distributions for slow CMEs (speed $\leqslant$ 400 km s^{-1}, panel (a)), mid-speed CMEs (400 km s^{-1} $<$ speed $\leqslant$ 800 km s^{-1}, panel (b)) and fast CMEs (speed $>$ 800 km s^{-1}, panel (c)). In the upper left corner of each panel, the basic parameters of these distributions are presented. Dashed lines represent a Gaussian fitting to histograms obtained from observations.

between solar cycles 23 and 24. In such an environment, CMEs could eject and expand more easily, but at the same time their internal magnetic field and density were rapidly rarefied and their trajectories were easily deformed (Gopalswamy et al. 2014, 2015). For the same reason, CMEs in cycle 24 disappeared more quickly from the LFOV than those in cycle 23.

It is known that slower ejections are more susceptible to trajectory deviations than fast ejections (e.g., Wang et al. 2004; Gui et al. 2011). Figure 3 presents the deflection distributions for slow CMEs (speed$\leqslant$ 400 km s^{-1}, panel (a)), mid-speed CMEs (400 km s^{-1} $<$ speed$\leqslant$ 800 km s^{-1}, panel (b)), and fast CMEs (speed$>$ 800 km s^{-1}, panel (c)). All deflections are normally distributed with peaks around 0°. As we might have guessed, we observe a systematic decrease in the FWHM of the distributions as the speed of the CMEs increases (from 14.°4 to 11.°8). This confirms earlier observations that slower ejections are more susceptible to trajectory deformations. It is worth noting, however, that distributions are very similar for low-speed and mid-speed CMEs. Only the fastest CMEs are less burdened by deflection.

The next parameter that affects deflections is CME apparent width. This parameter has not been widely discussed in studies so far. CMEs with larger angular widths are more likely to interact with different coronal magnetic structures. However, wider ejections are also more massive, and previous research shows (Kay et al. 2015) that more massive ejections are less susceptible to trajectory deviations. It seems that the influence of the angular width of the CMEs on the deflections may be more complex. In the CDAW catalog, the apparent angular width of CMEs is given for each CME. Figure 4 demonstrates the deflection distributions for CMEs with the angular width $>$ 30° (panel (a)), with the angular width $>$ 60° (panel (b)), and with the angular width $>$ 120° (panel (c)). All distributions, as usual, are normally distributed with peaks around 0°, but their FWHA systematically increases with the apparent angular width of events. The FWHM increases from 14.2 for all considered CMEs (Figure 2) to 17.°3 for the widest events (width $>$ 120°). It should be noted that the FWHM increase is not significant, especially when we compare FWHM for events with the angular width $>$ 60° and with the angular width $>$ 120°. It seems that, at a certain angular width, the masses of ejecta are so large that their inertia inhibits further deflection increase, due to the increase in their spatial dimensions. This issue will be discussed later in this article.

Individual CMEs may have different environments depending on the location. However, in terms of statistics (considering a large number of CMEs during a long period of time), location should not matter. Figure 5 shows the deflection distributions for CMEs with |latitude| $\leqslant$ 30° (panel (a)), with 30°$<$ |latitude| $<$ 60° (panel (b)), and |latitude| $\geqslant$ 60° CMEs (panel (c)). In contrast to the previous considered factors, we do not observe any change in distribution shape due to the different CME locations. All distributions have very similar parameters (upper left corners of the panels) and are almost normal distributions. The value and direction of the deflection for the considered period of time do not significantly depend on the CME location on the solar disk. However, we must remember that these distributions are cumulative for more than two solar cycles. The situation may change if we consider the different phases of the solar cycle. This is suggested by the slightly asymmetric distribution observed for CMEs near the equator

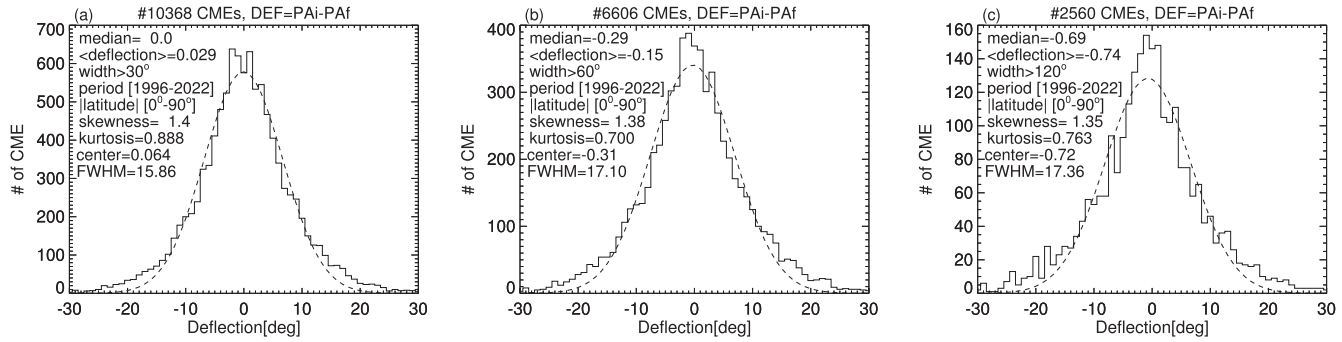

Figure 4. Deflection distributions for CMEs with the angular width >30° (panel (a)), with the angular width >60° (panel (b)), and with the angular width >120° (panel (c)). In the upper left corner of each panel, the basic parameters of these distributions are presented. Dashed lines represent a Gaussian fitting to histograms obtained from observations.

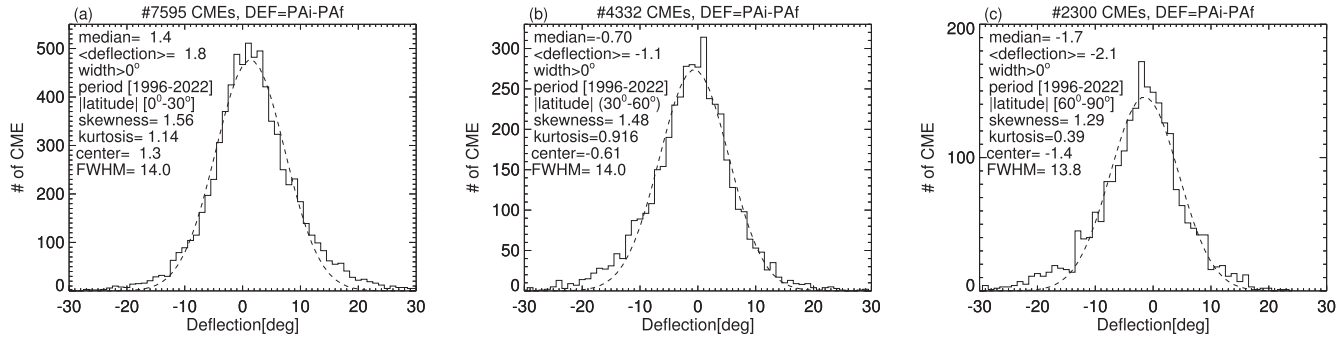

Figure 5. Deflection distributions for CMEs with |latitude| ⩽ 30° (panel (a)), with 30°<|latitude| < 60° (panel (b)) and |latitude| ⩾ 60° CMEs (panel (c)). In the upper left corner of each panel, the basic parameters of these distributions are presented. Dashed lines represent a Gaussian fitting to histograms obtained from observations.

(panel (a)) and near the pole (panel (c)). In the case of CMEs located close to the equator, it can be seen that the distribution has a long right tail. This means we are dealing with a right-skewed distribution (mean>median>center). For CMEs located close to the poles, the distribution has a long left tail. Therefore, there is a left-skewed distribution (center>median>mean). We may expect that CMEs with a low latitude deflect mostly toward the equator and those with a high latitude are deflecting mostly toward the solar poles. This finding needs a more detailed examination at different phases of solar activity. Such an analysis will be presented later in this paper.

3.2. Evolution of Deflection with Time

In the previous section, we considered the influence of CME basic parameters on their deflections. They covered the entire observation period. However, from previous studies, it is known that deflection in the solar corona is mainly caused by the magnetic field coronal holes. The CH occurrence and location depends on solar cycle phases. Therefore, we now focus on deflection changes along with solar activity cycles, thanks to a long series of observations carried out by the SOHO mission.

3.2.1. Deflection versus Solar Cycle Activity

Figure 6 presents the distributions of yearly averaged deflections (PAi-PAF) of all considered CMEs (panel (a)), CMEs from the northern hemisphere (panel (b)), and CMEs from the southern hemisphere (panel (c)). Light gray bars are separately for negative and positive deflection. Dark gray bars are for both kinds of deflection together. If this average is positive, it means that in a given year we have more events deflecting toward the equator than those deflecting toward the poles. In the case of a negative value, the situation is reversed. Predictably, the deflection distribution mimics solar activity cycles. This is clearly visible in panel (a). In periods of minimum solar activity, the yearly averaged values of deflections are positive (equatorward), while during maxima, they are negative (poleward). This is consistent with the location of coronal holes during these periods of solar activity. During solar activity minima, near the poles, we observe two prominent coronal holes, which deflect the CME primarily toward the equator. During periods of increased activity, coronal holes appear frequently near the equator, causing mostly negative CME deflection. However, during this period, coronal holes can also be located at different solar latitudes, so they can deflect CMEs both toward the equator and the poles. Therefore, the average positive deflection during periods of minimum solar activity ($\langle$deflection $\rangle \approx 5°$) is in absolute value twice as large as the average negative deflection during periods of increased solar activity ($\langle$deflection $\rangle \approx 2°$). Another finding, which we have already described in the previous subsections, is that the absolute values of the minimum and maximum deflection in cycle 24 are clearly larger than those in cycle 23. This confirms our observations regarding the difference in the FWHM for deflection distribution in both solar activity cycles. This means that CMEs in cycle 24 are much more easily deflected than those in cycle 23. It is also worth nothing that the average values of deflection range from $-2.^{\circ}5$ to 5°, but the separate average values for positive and negative deflections, in a given year, may be much higher (from $-10°$ up to 10°). The next interesting result comes from an analysis of the remaining panels ((b) and (c)) in Figure 5. They show the evolution of the deflection distribution with solar activity cycles but for

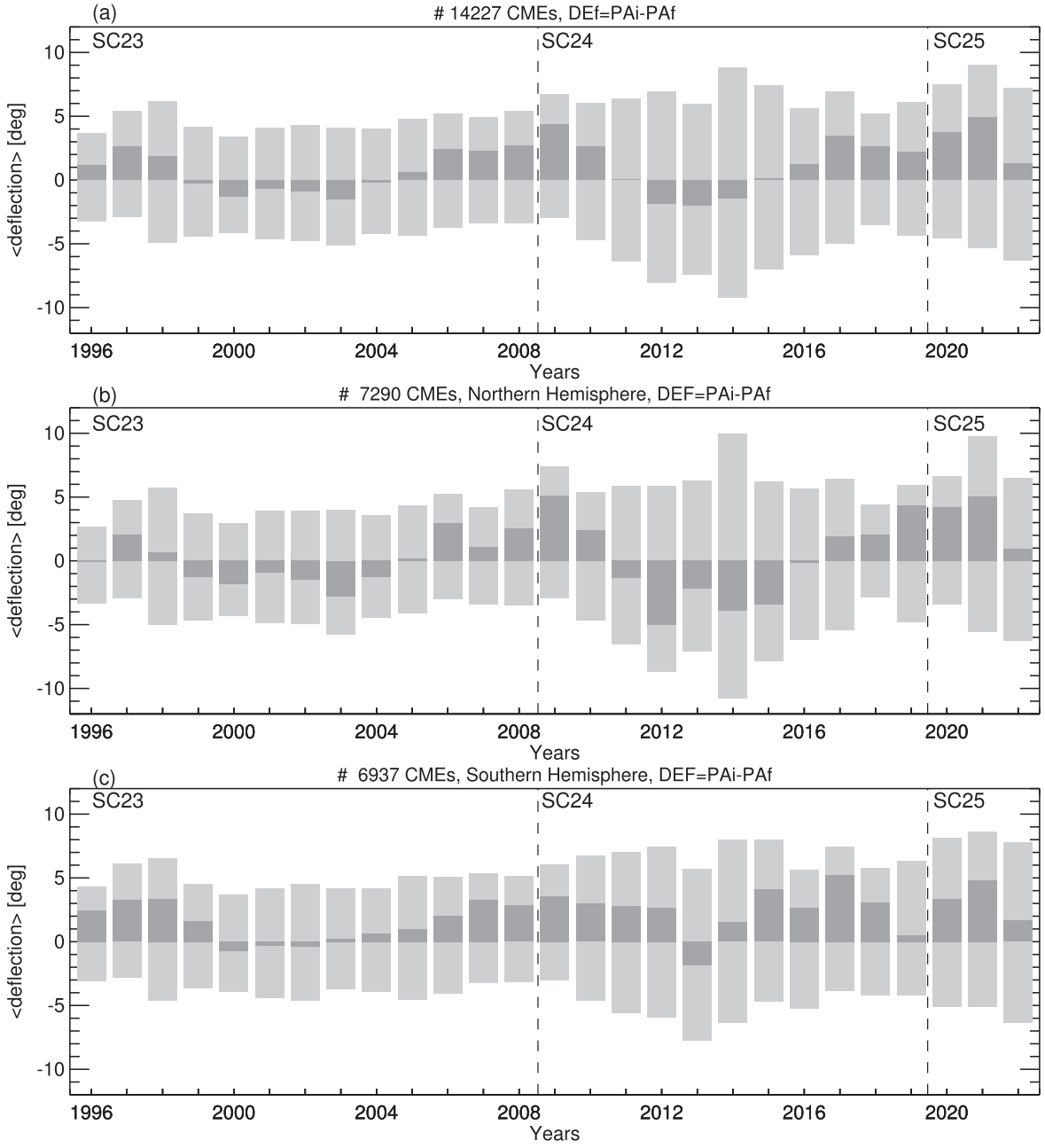

Figure 6. Distributions of yearly averaged deflections (PAi-PAF) of all considered CMEs (panel (a)), CMEs from the northern hemisphere (panel (b)), and CMEs from the southern hemisphere (panel (c)). Light gray bars represent negative and positive deflection separately. Dark gray bars are for both kinds of deflection together. The dashed vertical lines represent solar cycle boundaries.

ejections appearing in the northern and southern hemispheres. There is clear asymmetry between both hemispheres. In the northern hemisphere, the deflection distribution clearly tracks solar activity cycles. In solar activity maxima, we observe negative deflection values, while in solar activity minima, positive deflection is clearly visible (panel (b)). But for the southern hemisphere (panel (c)), practically throughout the entire solar activity cycle, with the exception of one year (2013), the yearly averaged deflections are positive. It looks like the southern hemisphere in cycle 24 was dominated by the polar magnetic field. Gopalswamy (2016, 2018) have shown a severe north–south asymmetry in the polar microwave brightness, which is a proxy for the polar magnetic field strength. Similar asymmetry in the polar field evolution around polar reversal in cycle was found also by Petrie (2022). The north polar reversal commenced earlier (two year earlier), but completed later than the south polar reversal. The north magnetic field remained close to zero for several years. During this time, the south magnetic field reversed very quickly and swiftly strengthened the reversed magnetic field. It was not until two years after the reversal of the magnetic field at the south pole that the reversal of the magnetic field at the north pole began to strengthen. Such an asymmetric evolution of magnetic fields has never been observed previously although the rush-to-the-pole phenomenon from historical records indicates such occurrences in the past (see Figure 9 of Gopalswamy 2018). The evolution of the photospheric magnetic field can be traced on freely available synoptic

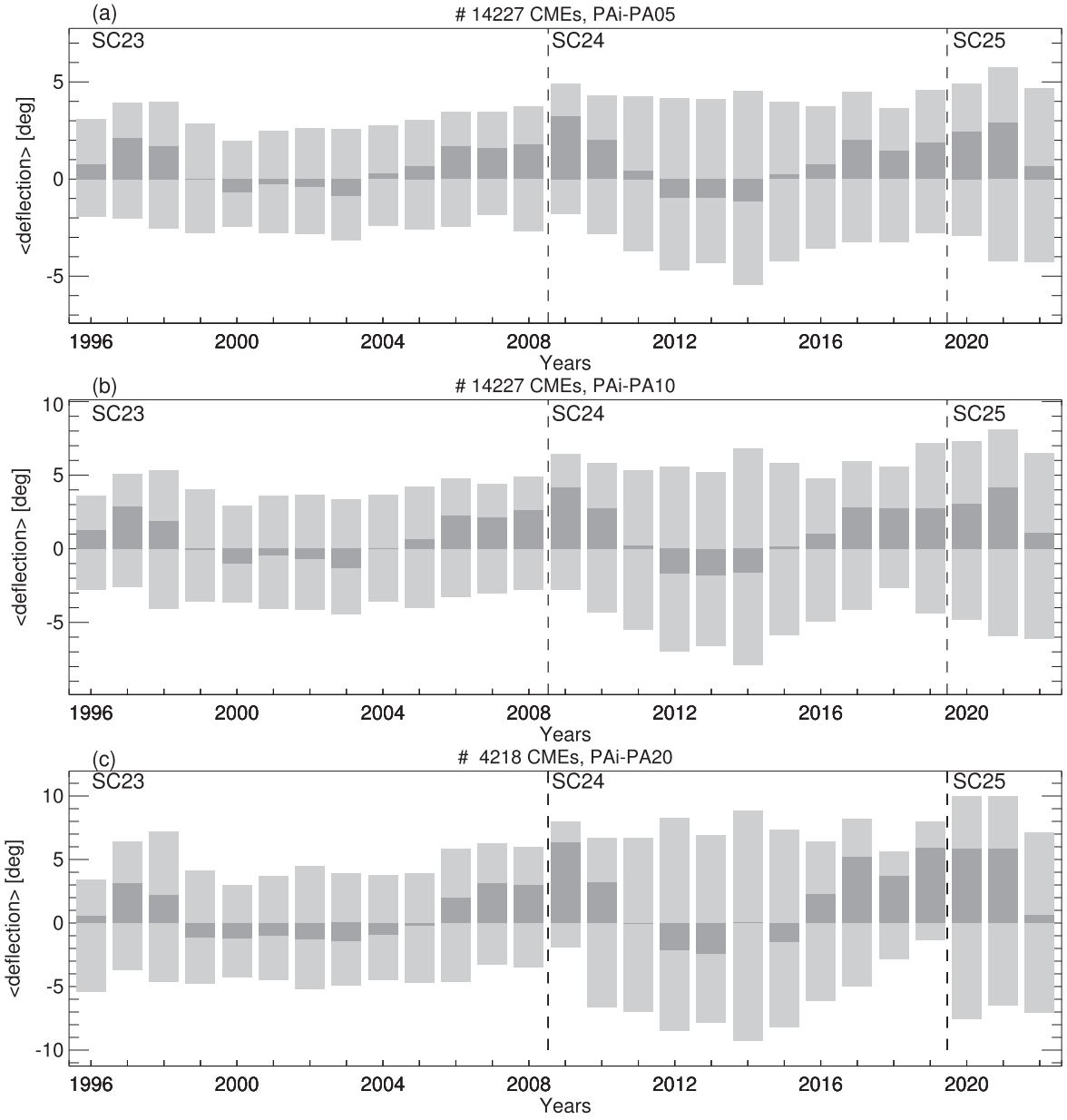

Figure 7. Distributions of yearly averaged deflection at $5R_{\odot}$ (panel (a)), at $10R_{\odot}$ (panel (b)), and at $20R_{\odot}$ (panel (c)). Light gray bars represent negative and positive deflection separately. Dark gray bars are for both kinds of deflection together. The dashed vertical lines represent solar cycle boundaries.

photospheric magnetic field maps (e.g., https://solarscience.msfc.nasa.gov/images/magbfly.jpg.) The described behavior of the polar magnetic field is reflected in the evolution of deflection during the 24th solar activity cycle. In the northern hemisphere, we saw a switch of deflection from positive to negative in 2011, during the magnetic field reversal period in the northern hemisphere. This is due to the appearance of low-latitude coronal holes or lack of polar coronal holes when the solar maximum begins around 2011. The reversal happens at the end of the maximum phase, also marking the growth of polar field of the new polarity. The deflection remained negative throughout the period when the polar magnetic field was close to zero (dominance of the equatorial field). This is due to anti-Hale plumes going to the poles that prevented reversal. Only in 2016, when the reverse magnetic field strengthens, does the deflection becomes positive again (dominance of the polar field). In the case of the southern hemisphere, only in one year (2013, two years after turning the field in the northern hemisphere) did we record a negative deflection (dominance of the equatorial field). Because the inverted field was strengthened very quickly, in 2014 it began to dominate and the deflection became positive again (dominance of the polar field). It is significant that the deflection, determined in this way, seems to be closely related to the structure of the global magnetic field. It should be noted, however, that the research carried out by MacQueen et al. (1986) suggests that the overall bipolar magnetic field of the Sun during solar minimum may be responsible for the deflection.

3.2.2. Deflection with Distance from the Sun

The large FOV of LASCO coronagraphs allowed us to study not only the CME's deflection value, but also its change with distance from the Sun. Figure 7 shows the distributions of

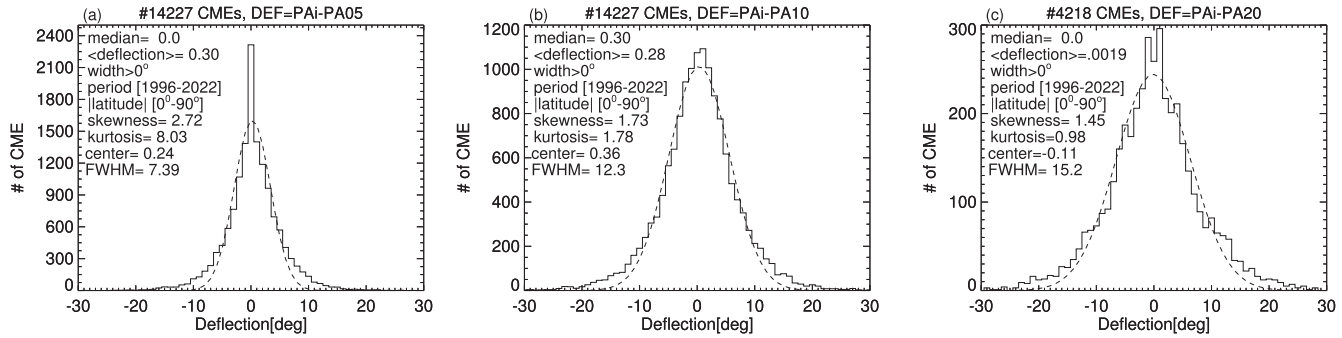

Figure 8. Deflection distributions of all considered CMEs for PAi-PA05 (panel (a)), PAi-PA10 (panel (b)), and PAi-PA20 (panel (c)).

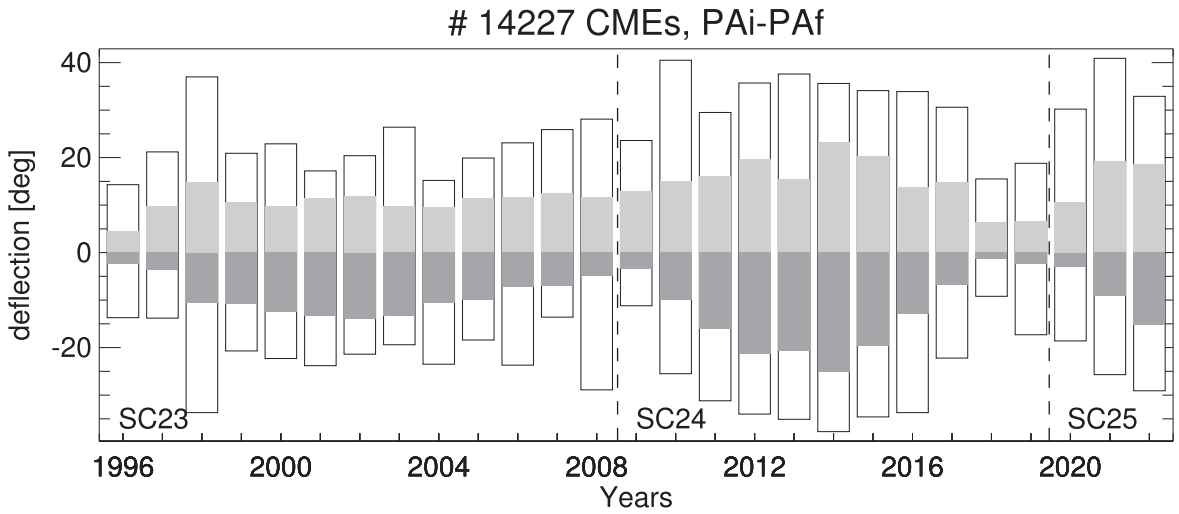

Figure 9. Distributions of yearly averaged deflections—but only for 50 of the most deflected CMEs in a given year (light gray is for positive deflection and dark gray is for negative deflection). The white boxes show the maximal and minimal deflections recorded in a given year.

yearly averaged deflection at successive distances from the Sun (at $5\,R_\odot$, $10\,R_\odot$, and $20\,R_\odot$). Light gray bars represent negative and positive deflection separately. Dark gray bars are for both kinds of deflection together. In general, the distributions visible in the figure are similar to those presented in the previous figure. They reflect solar activity cycles very well. It can be seen that, at a distance of $5R_\odot$, the deflection is clearly visible (panel (a)). However, it increases systematically with the distance from the Sun. Negative and positive peaks of the distributions in successive phases of solar cycles increase systematically from panel (a) to panel (b). It is clear that deflection increases with distance from the Sun and can be significant in the LFOV. To estimate this evolution with distance, we analyzed the deflection distributions of CMEs at the different heights from the Sun.

Figure 8 displays the distribution of all considered CMEs at successive distances from the Sun (at $5\,R_\odot$, $10\,R_\odot$, and $20\,R_\odot$, respectively). When analyzing these distributions, two very interesting features should be noted. First, the deflection distribution at $5\,R_\odot$ is not normally distributed. The kurtosis for this distribution is 8.01, which means the distribution is leptokurtic. It therefore has the Laplace (exponential) rather than the Gaussian distribution. This means that, near the Sun, deflection (which is a random process) occurs in a significantly heterogeneous magnetic medium (CHs, active regions, streamers). Farther from the Sun (after passing $5\,R_\odot$), the medium becomes homogeneous and deflection assumes a normal distribution (distributions for distances $10\,R_\odot$ and $20\,R_\odot$). Considering CME deflection allows us to distinguish physical processes determining the ejection trajectory near the Sun. The second significant result is the systematic increase in the FWHM with increasing distance from the Sun. The FWHM for distances $5\,R_\odot$, $10\,R_\odot$, and $20\,R_\odot$ are $7\overset{\circ}{.}4$, $12\overset{\circ}{.}3$, and $15\overset{\circ}{.}2$, respectively. This means that, in the field of view of LASCO coronagraphs, on average, the deflection increases linearly with the distance from the Sun (the slope of the linear fit is 0.5). Thus, deflection of CMEs is a continuous process not limited to the close vicinity of the Sun. This is also a common process. From the last distribution (panel (c), using the FWHM) we can deduce that the 24% of CMEs reaching a distance of $20\,R_\odot$ have an absolute deflection of $>7\overset{\circ}{.}6$.

3.2.3. Deflection Limits

In the previous sections, we analyzed the yearly averaged deflections. The analysis conducted in this way enabled us to study general trends in CME trajectories for specific periods of time. Currently, we want to consider the limit values reached by deflection in the LFOV. Figure 9 shows distributions of yearly averaged deflections—but only for 50 of the most deflected CMEs in a given year. The positive deflected CMEs are represented by light gray bins, while the negative deflected CMEs are presented by dark gray bins, respectively. In addition, the white boxes show the maximal and minimal deflections recorded in a given year. In the figure, we can observe some characteristic features. Throughout the time period under consideration, CMEs undergo both positive and

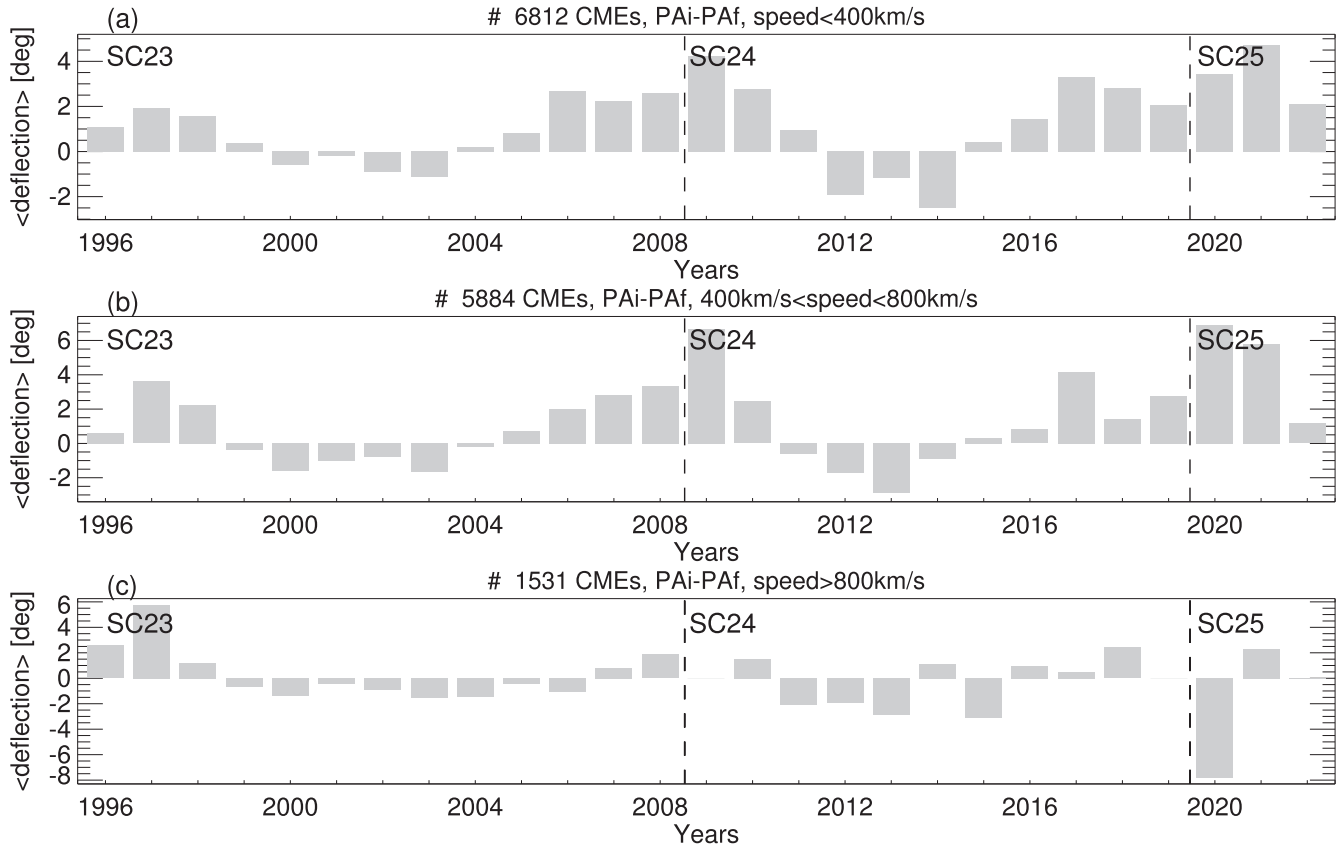

Figure 10. Distributions of yearly averaged deflection for slow CMEs (speed $\leqslant$ 400 km s^{-1}, panel (a)), mid-speed CMEs (400 km s^{-1} $<$ speed $\leqslant$ 800 km s^{-1}, panel (b)), and fast CMEs (speed $>$ 800 km s^{-1}, panel (a)).

negative deflections. However, in periods of solar minima (1996–1997, 2007–2009, and 2017–2020), it can be seen that the average value of positive deflection is definitely higher than the negative one. During periods of high solar activity, when negative deflection dominates, this difference in favor of negative deflection is not so significant. This means that, during periods of maximum solar activity, we observe a similar number of CMEs undergoing strong negative and positive deflection. It is also clear that CMEs in solar cycle 23 are less prone to strong deflection than those observed in cycle 24. The average values of negative and positive deflection for the most deflected CMEs in cycle 23 are in the range $\pm 15°$, and in cycle 24 this range extends to $\pm 20°$. This is also confirmed by comparing the maximal and minimal deflection values recorded in both cycles. Maximal and minimal deflection values, with the exception of 1998, are within $\pm$ 30° for cycle 23 and $\pm$ 40° for cycle 24, respectively. These results are consistent with those obtained from CMEs associated with prominence eruptions (e.g., Gopalswamy et al. 2012; Gopalswamy 2018). The first three years of cycle 25 mimic cycle 24's early phase deflection behavior. This figure shows that a large group of CMEs can undergo very strong deflections of up to 40°. It should be remembered that our considerations are affected by projection effects; therefore, the deflection values we determined are only lower limits.

3.3. Deflection versus Speed

In previous subsections, we showed that deflection depends on CME speed. It decreases especially for the fast ejections (speed $>$ 800 km s^{-1}). Now we analyze the effect of speed on deflection in solar activity cycles. Figure 10 shows the distribution of yearly averaged CME deflections separately for low-speed, mid-speed, and fast events. Regardless of CME

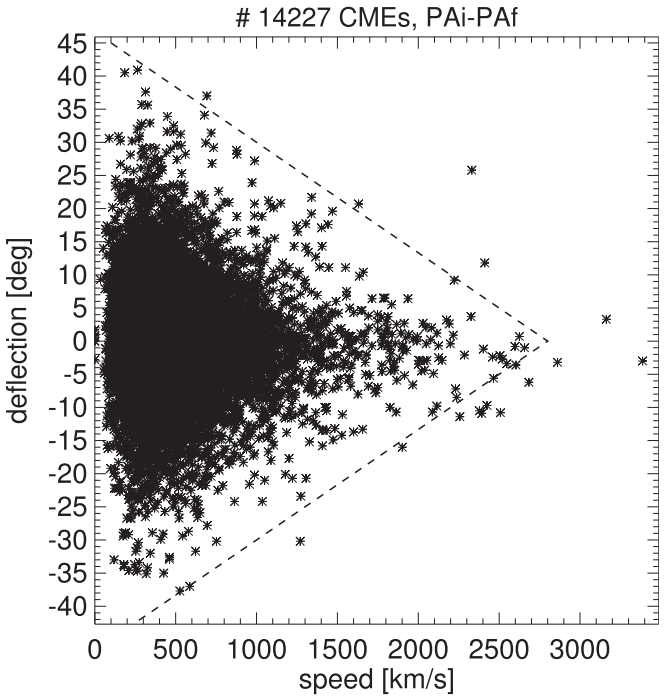

Figure 11. Scatter plot of deflection vs. speed for all considered CMEs. The dashed ones show roughly the limiting deflection values for the individual ejection velocities.

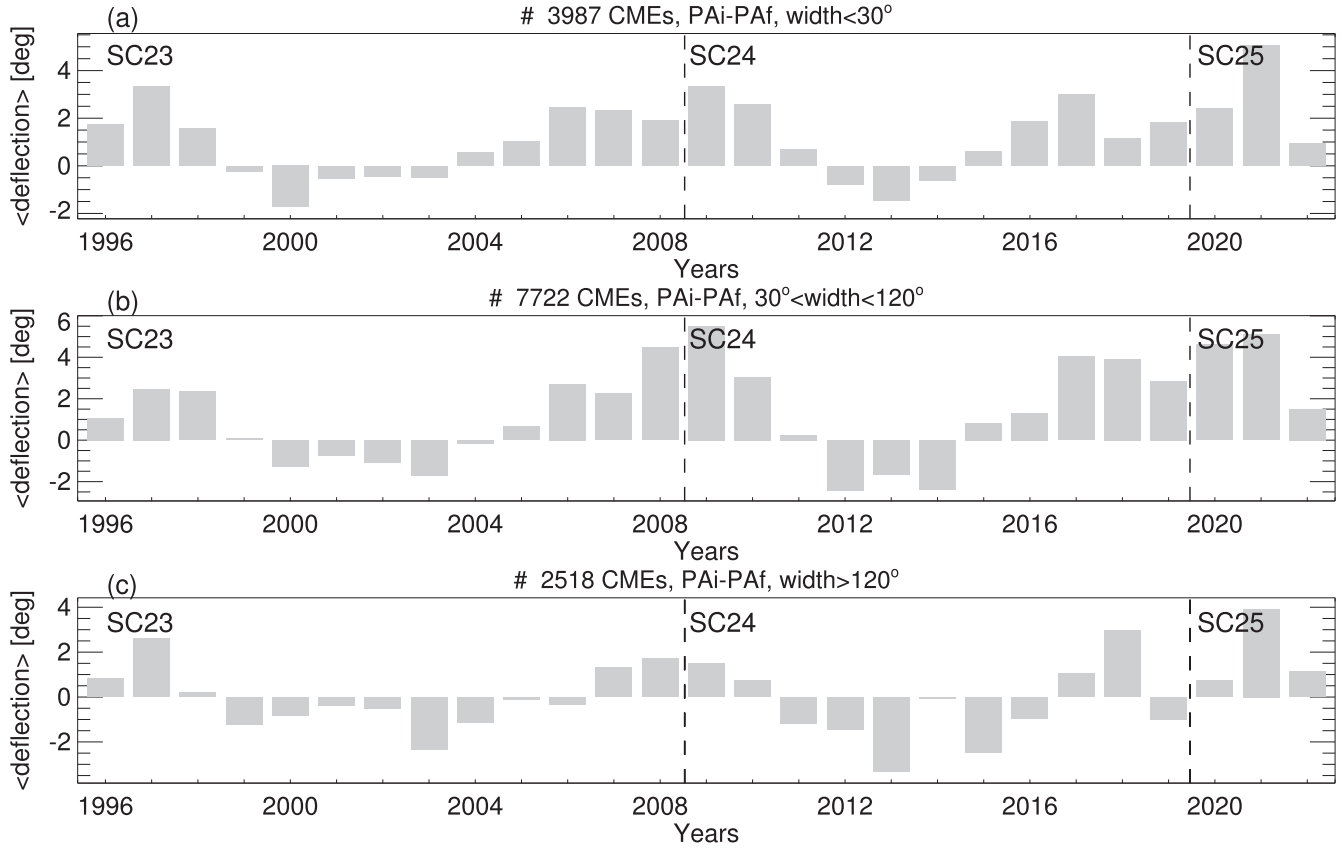

Figure 12. Distributions of yearly averaged deflection for narrow CMEs (widthle30°, panel (a)), mid-width CMEs (30° < widthle120°, panel (b)), and wide CMEs (width >120°, panel (a)).

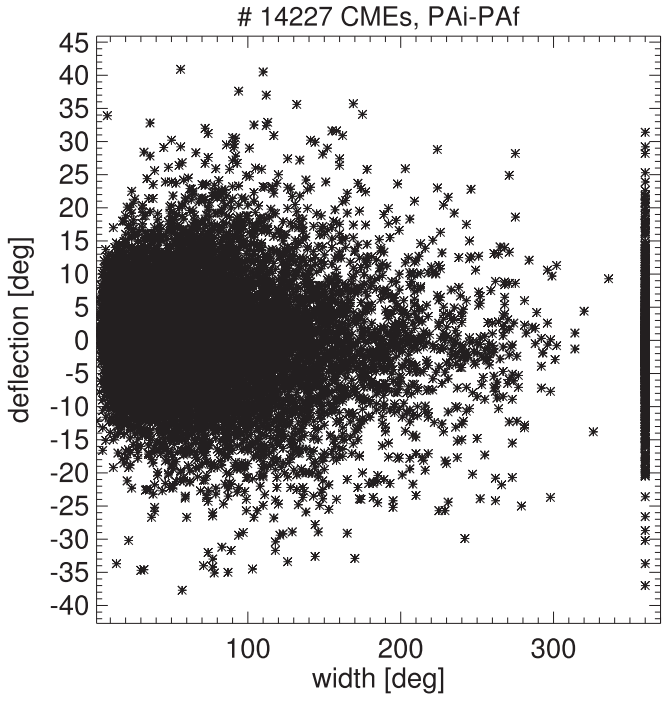

Figure 13. Scatter plot of deflection vs. width for all considered CMEs.

speed, the distribution of yearly averaged deflection follows solar activity cycles. For slow and mid-speed events, the distributions are very similar. We do not observe a decrease in deflection in these speed ranges. Throughout the observed period, the yearly averaged deflection is in the range of [−3°, 4°] and [−3°, 6°] for slow and mid-speed CMEs, respectively. In the case of the fastest events, we can observe a decrease in the average deflection. It is, with the exception of two years (1996, 2020), within the range of [−2°, 2°]. This trend is more recognizable in Figure 11, which shows the scatter plot of deflection versus speed for all events considered in this study. The dotted lines indicate deflection limits depending on CME speed. It can be clearly seen that the maximum deflection values decrease significantly with CME speed. Only slow ejections can undergo strong deflection (±40°) near the Sun. Very fast ejections that are potentially geoefficient undergo significantly smaller deflections of ±10°.

3.4. Deflection versus Width

As mentioned earlier, deflection dependence on CME angular width may be complex. The increase in the angular width of the CME, which increases the probability of interaction with the magnetic structures observed in the corona, simultaneously causes an increase in the mass of the CME, which increases the inertia of the events and weakens their susceptibility to deflection of their trajectories. Figure 12 displays the distributions of yearly averaged deflection for narrow, mid-width, and wide CMEs. These three distributions, regardless of CME width, track solar activity cycles. There are also no significant differences between these distributions. It is worth noting that the yearly averaged deflections for mid-width CMEs fall within a slightly larger range [−2°, 6°] than the distributions for narrow and wide CMEs [−2°, 4°]. This means that the deflection slightly increases with CME width, but only

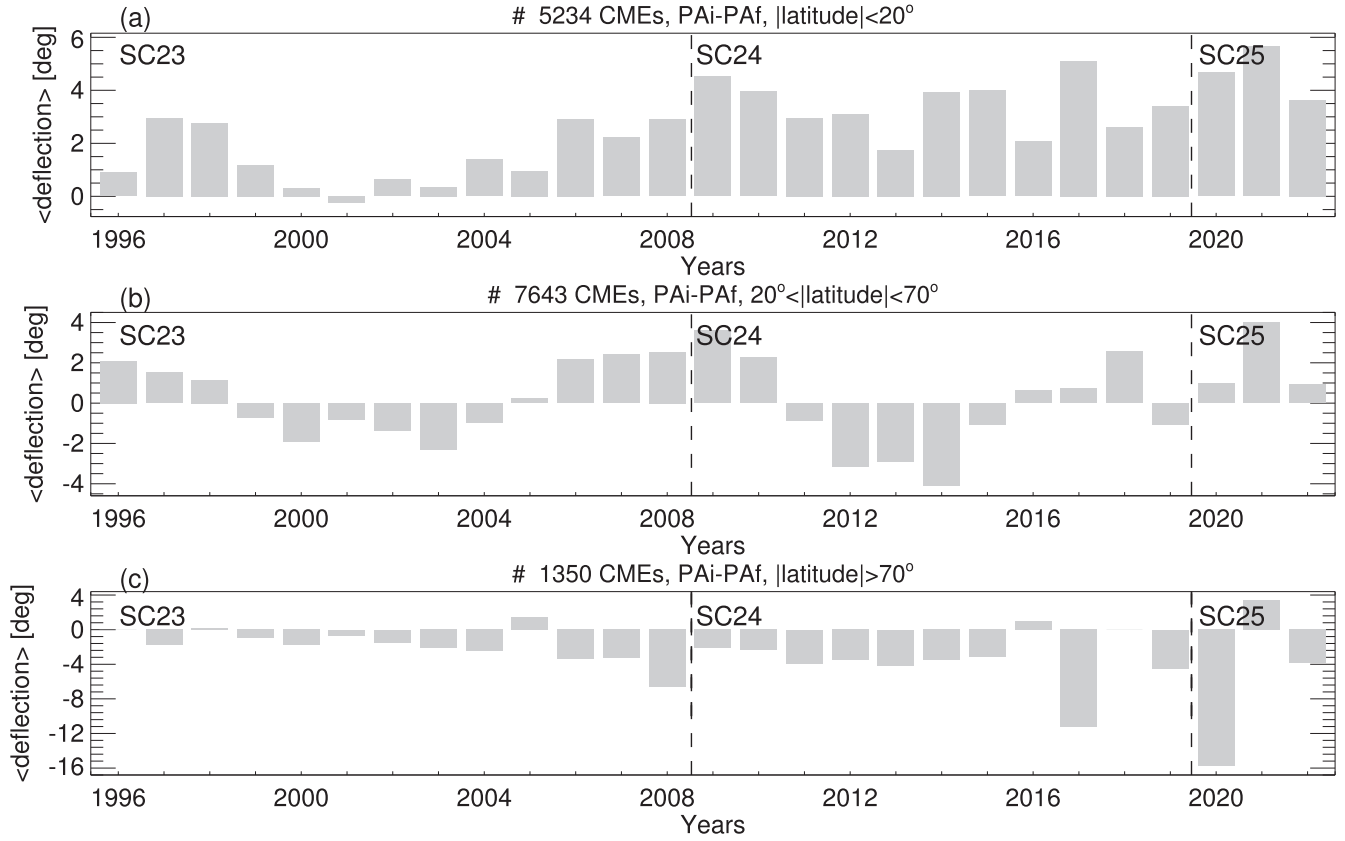

Figure 14. Distributions of yearly averaged deflection for CMEs with |latitude| $\leqslant 20°$ (panel (a)), CMEs with $20° <$ |latitude| $\leqslant 79°$ (panel (b)), and CMEs with |latitude| $> 70°$, panel (a)).

up to certain apparent width values. Those massive events are less prone to deflection. This is also confirmed by the observation of average deflection at solar activity minima and maxima. During periods of minimum solar activity, we observe moderately positive deflection. However, it is markedly higher for narrow (panel (a)) and mid-width CMEs (panel (b)) than for wide ejections (panel (c)). On the other hand, during periods of maximal solar activity, the absolute value of deflection is larger for wide CMEs (panel (c)) than for narrow (panel (a)) and mid-width CMEs (panel (b)). It can be inferred that, at minimum when the strength of background magnetic field is low, wide CMEs are not prone to trajectory deviation like mid-width or narrow CMEs. During these phases of solar activity, wide CME trajectories are determined mainly by their high inertia. On the other hand, in periods of high solar activity, when the background magnetic field strength is more prominent, they can be more significantly deflected than narrow and mid-width events. During these phases of solar activity, wide CME trajectories are dominated by interactions with strong magnetic structures present in the solar corona at that time.

Similar conclusions can be drawn from analyzing Figure 13. It shows a scatter plot of deflection versus CME width. Narrow ejections, whose probability of interaction with magnetic structures present in the solar corona is not large, are not significantly deflected. Their maximal deflection angles are within $\pm 20°$. As the CME width increases, the maximum deflection increases as well. The largest deflection can be expected for CMEs having angular widths in the range [60°,120°]. For CMEs with a width above 120°, the deflection decreases. For the widest events, it is within $\pm 20°$. Very interesting is the deflection range noted for halo events for which, due to the projection effect, the spatial angular width cannot be determined. Deflection for halo events extends over a wide range $\pm 20°$, similarly to ejections with angular widths around 90°. This may suggest that not all halo events are very wide, as their apparent widths are similar to mid-width CMEs considered in this study.

3.5. Deflection versus Position Angle

The third critical parameter that affects the extent of deflection is the location of CME on the solar disk as determined by the latitude or CPA. Figure 14 shows the distribution of yearly averaged deflections for CMEs at different absolute latitudes. For the CME originating close to the equator (|latitude| $\leqslant 20°$, panel (a)), the yearly averaged deflection assumes positive values for almost the entire period under discussion (except for the year 2001). This trend increases over time. At the minimum of solar activity in cycles 23, 24, and 25, the maximum values of the yearly averaged deflection reached values of $\approx 2\overset{\circ}{.}5$, $4\overset{\circ}{.}5$, and almost 6°, respectively. A similar tendency is also observed in periods of higher solar activity. A completely opposite picture is observed for CMEs located close to the poles (|latitude| $> 70°$, panel (b)). During almost the entire period under discussion (except 2005), for these ejections the yearly averaged deflection took negative values. This trend clearly increases with time. In the minimum of solar activity in cycles 23, 24, and 25, the minimum values of the yearly averaged deflection reached values of $\approx -4\overset{\circ}{.}0$, $-6\overset{\circ}{.}5$, and almost $-16°$, respectively. A similar tendency is also observed in periods of higher solar activity. This means that CMEs that form near the equator are

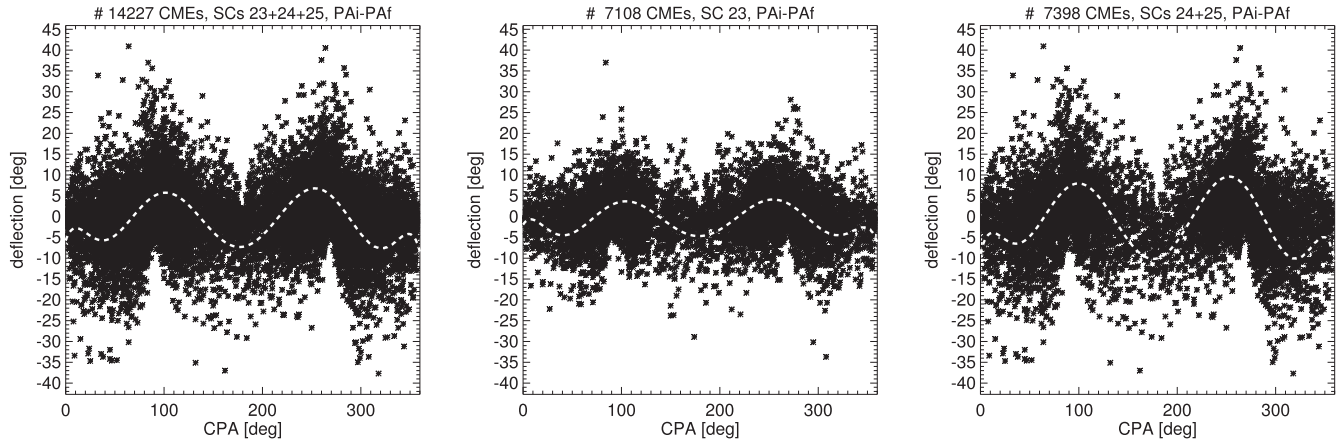

Figure 15. Scatter plots of deflection vs. CPA for all considered CMEs, for CMEs recorded in SC23, and for CMEs recorded in SC 24 and 25. Dashed lines represent polynomial fits to the data points.

mostly deflected equatorward (regardless of the phase of the solar cycle) and those that form at high latitudes near are deflected poleward (regardless of the phase of the solar cycle). It is very significant that these trends increase with subsequent cycles (from 23 to 25). We may suppose that the Sun's magnetic field structure undergoes systematic evolution superimposed on 11 yr cycles. Only CMEs appearing in the middle zone ($20° < |\text{latitude}| \leqslant 80°$, panel (b)) are deflected according to the phases of the solar cycle and according to the distribution of CHs in the Sun (where low solar activity corresponds to positive deflection, and high solar activity to negative deflection).

Similar conclusions can be drawn from Figure 15, which shows scatter plots of deflection versus CPA for all considered CMEs as well as separately for those observed in SC 23 and in SCs 24 and 25. Dashed lines represent a polynomial fit to the observation points. There are clear deflection changes with the CME position on the solar disk. CMEs appearing near the equator (CPA = 90° and 270°) are visibly deflected mainly toward it (positive deflection), while those formed near the poles (CPA = 0°, 180° or 360°) are directed toward them (negative deflection). Analyzing these scatter plots for both cycles of solar activity, it can be seen that the average amplitude of deflection changes with the CPA (dotted lines amplitudes) is twice as large in cycle 23 (±5° compared to cycles 24 and 25 (±10°).

4. Summary and Discussion

In the present study, we performed an extensive statistical analysis of CME deflections in the LFOV. These studies are relevant because one of the most significant factors determining CME geoefficiency is their trajectory (direction and arrival time). For this purpose, we utilized manual height–time measurements made for the CDAW catalog. Using these measurements, we study the evolution of deflection with distance from the Sun. In addition, thanks to a very long series of observations from the SOHO mission, we studied the evolution of CME deflections along with solar activity cycles. We must note that coronagraphic observations are subjected to projection effects, and therefore the deflection values estimated in these studies should be considered as lower limits. The following are the main conclusions.

1. CME deflection in the LFOV is a common phenomenon, and in many cases it can be very significant (the FWHM of deflection distribution for all considered CMEs is 14°.3).
2. The time evolution of the yearly averaged deflections follows activity cycles very well. During solar activity minima, the average deflection is equatorward, and during maxima, it is poleward. In addition, the absolute values of the mean deflection are much more pronounced during solar activity minima than those determined during periods of high solar activity. The described trends are consistent with the common assumption that CHs are the main source of deflection of CMEs in the vicinity of the Sun.
3. It turns out that the average deflection value in the last three decades has steadily increased. The average values of negative and positive deflection for the most deflected CMEs in cycle 23 were within ±15° and in cycle 24 were within ±20°. The maximum deflection values recorded in both cycles differed by a factor of two. This may mean that, on the Sun, in addition to cyclical 11 yr changes, there are other systematic changes in the global magnetic field as well.
4. This thesis can be confirmed by the never-before-recorded asymmetric process of reversing the magnetic field observed in opposite solar hemispheres (Gopalswamy 2016, 2018; Petrie 2022). This asymmetric reversal was also clearly visible in solar cycle 24 deflection behavior. Interestingly, the deflection determined in the current study mimics the global solar magnetic structure.
5. Using the deflection distributions at selected distances from the Sun, it was shown that the deflection increases linearly with distance from the Sun (slope factor 0.5 within LFOV). In the closest (up to 5 $R_\odot$) vicinity of the Sun, the deflection has an exponential distribution. This means that, near the Sun, deflection occurs in a significantly heterogeneous magnetic medium (with CHs, active regions, and streamers). Farther from the Sun, the medium becomes homogeneous and deflection assumes a normal distribution.
6. Deflection is weakly dependent on CME speed. Only very fast ejections (speed $> 1500\,\mathrm{km\,s^{-1}}$) are not subject to significant deflection.

7. The dependence of deflection on CME apparent width is more complex. An increase in the angular width of the CMEs generates two opposing effects affecting the extent of deflection (an increase in the probability of interaction with the magnetic structure of the solar corona and simultaneously an increase in mass and thus inertia of ejections).
8. The deflection significantly depends on the CME latitude. CMEs originating at high latitudes are mostly deflected poleward, but those originating close to the solar equator are mostly deflected equatorward. Only CMEs appearing in the middle zone are deflected according to the phases of the solar cycle and according to the distribution of CHs in the Sun (where low solar activity corresponds to positive deflection, and high solar activity to negative deflection).
9. In our univariate analysis, we showed that deflection is not linearly correlated with speed, angular width, or position angle. To fully understand these relationships, we also performed a multivariate statistical analysis. For this purpose, we used the statistical multiple linear regression approach where CME deflection angle is the sum of linear coefficients of the four independent variables (speed, angular width, solar latitude, and distance from the Sun). This analysis confirmed univariate results. The resulting multiple linear regression coefficients are close to zero, the respective correlation coefficients are below 0.2, and a multiple correlation coefficient (R) is equal to 0.27.

Acknowledgments

This work was supported by NASA's LWS program.

ORCID iDs

Grzegorz Michalek https://orcid.org/0000-0001-6848-971X
Nat Gopalswamy https://orcid.org/0000-0001-5894-9954
Seiji Yashiro https://orcid.org/0000-0002-6965-3785

References

Brueckner, G. E., Howard, R. A., Koomen, M. J., et al. 1995, SoPh, 162, 357
Cremades, H., & Bothmer, V. 2004, A&A, 422, 307
Feng, X., Wu, S. T., Wei, F., & Fan, Q. 2003, SSRv, 107, 43
Gómez, J. M. R., Palacios, J., Vieira, L. E. A., & Lago, A. D. 2019, ApJ, 884, 88
Gómez, J. M. R., Vieira, L., Lago, A. D., & Palacios, J. 2018, ApJ, 852, 137
Gopalswamy, N. 2016, GSL, 3, 8
Gopalswamy, N. 2018, in Extreme Events in Geospace, ed. N. Buzulukova (Amsterdam: Elsevier), 37
Gopalswamy, N., Akiyama, S., Yashiro, S., et al. 2014, GeoRL, 41, 2673
Gopalswamy, N., Akiyama, S., Yashiro, S., Michalek, G., & Lepping, R. P. 2008, JASTP, 70, 245
Gopalswamy, N., Lara, A., Yashiro, S., & Howard, R. A. 2003a, ApJL, 598, L63
Gopalswamy, N., Mäkelä, P., Xie, H., Akiyama, S., & Yashiro, S. 2009, JGRA, 114, L63
Gopalswamy, N., Nunes, S., Yashiro, S., & Howard, R. 2004, AdSpR, 34, 391
Gopalswamy, N., Shimojo, M., Lu, W., et al. 2003, ApJ, 586, 562
Gopalswamy, N., & Thompson, B. J. 2000, JASTP, 62, 1457
Gopalswamy, N., Xie, H., Akiyama, S., et al. 2015, ApJL, 804, L23
Gopalswamy, N., Xie, H., Yashiro, S., et al. 2012, SSRv, 171, 23
Gopalswamy, N., Yashiro, S., Kaiser, M. L., Howard, R. A., & Bougeret, J. L. 2001, ApJL, 548, L91
Gopalswamy, N., Yashiro, S., Liu, Y., et al. 2005, JGRA, 110, A09S15
Gopalswamy, N., Yashiro, S., Michalek, G., et al. 2009b, EM&P, 104, 295
Gui, B., Shen, C., Wang, Y., et al. 2011, SoPh, 271, 111
Harrison, R. A., Davies, J. A., Barnes, D., et al. 2018, SoPh, 293, 77
Hildner, E. 1977, in Astrophysics and Space Science Library, Vol. 71, Study of Travelling Interplanetary Phenomena, ed. M. A. Shea, D. F. Smart, & S. T. Wu (Dordrecht: Reidel), 3
Howard, R., Moses, J., Vourlidas, A., et al. 2008, SSRv, v.136, 136
Isavnin, A., Vourlidas, A., Kilpua, E. K. J., et al. 2013, SoPh, 284, 203
Isavnin, A., Vourlidas, A., Kilpua, E. K. J., et al. 2014, SoPh, 289, 2141
Kaiser, M. L., Kucera, T. A., Davila, J. M., et al. 2008, SSRv, 136, 5
Kay, C., & Gopalswamy, N. 2017, AGUFM, 2017, SH51E-03
Kay, C., Opher, M., Colaninno, R. C., Vourlidas, A., et al. 2016, ApJ, 827, 70
Kay, C., Opher, M., Evans, R. M., et al. 2015, ApJ, 805, 168
Liu, Y., Davies, J. A., Luhmann, J. G., et al. 2010a, ApJL, 710, L82
Liu, Y., Shen, F., & Yang, Y. 2019, ApJ, 887, 150
Liu, Y., Thernisien, A., Luhmann, J. G., et al. 2010b, ApJ, 722, 1762
Lugaz, N., Farrugia, C. J., Davies, J. A., et al. 2012, ApJ, 759, 68
Lugaz, N., Hernandez-Charpak, J. N., Roussev, I. I., et al. 2010, ApJ, 715, 493
Lugaz, N., Temmer, M., Wang, Y., & Farrugia, C. J. 2017, SoPh, 292, 64
MacQueen, R. M., Hundhausen, A. J., & Conover, C. W. 1986, JGR, 91, 31
Mäkelä, P., Gopalswamy, N., Xie, H., et al. 2013, SoPh, 284, 59
Manchester, W. B., Gombosi, T. I., Roussev, I., et al. 2004, JGRA, 109, A02107
Mishra, W., Wang, Y., Srivastava, N., & Shen, C. 2017, ApJS, 232, 5
Petrie, G. J. D. 2022, ApJ, 941, 142
Prise, A. J., Harra, L. K., Matthews, S. A., Arridge, C. S., & Achilleos, N. 2015, JGRA, 120, 1566
Rodriguez, L., Mierla, M., Zhukov, A. N., West, M., & Kilpua, E. 2011, SoPh, 270, 561
Shen, C., Wang, Y., Gui, B., Ye, P., & Wang, S. 2011, SoPh, 269, 389
Shen, F., Shen, C., Zhang, J., et al. 2014, JGRA, 119, 7128
Tousey, R. 1973, in Space Research XIII 2, ed. M. J. Rycroft & S. K. Runcorn (Berlin: Academie-Verlag), 713
Wang, Y., Chen, C., Gui, B., et al. 2011, JGRA, 116
Wang, Y., & Colaninno, R. 2014, ApJL, 784, L27
Wang, Y., Shen, C., Wang, S., & Ye, P. 2004, SoPh, 222, 329
Xiong, M., Zheng, H., & Wang, S. 2009, JGRA, 114, A11101
Xiong, M., Zheng, H., Wang, Y., & Wang, S. 2006, JGRA, 111, A11102
Yashiro, S., Gopalswamy, N., Michalek, G., et al. 2004, JGR, 109, A07105
Zhou, Y., & Feng, X. 2017, JGRA, 122, 1451
Zhou, Y. F., & Feng, X. S. 2013, JGRA, 118, 6007
Zhuang, B., Wang, Y., Hu, Y., et al. 2019, ApJ, 876, 73